ADVANCED MATERIALS
www.advmat.de

Electrode-Dependent and Tunable Sub-to-Super-Linear Responsivity in Mott Material-Enabled Near-Infrared Photodetectors for Advanced Near-Sensor Image Processing

*Bowen Li, Pengshan Xie, Baojie Chen, You Meng, Weijun Wang, Mingwei Yang, Boxiang Gao, Quan Quan, Yan Yan, Mingqi Ding, Danfeng Li, Chi Hou Chan, and Johnny C. Ho**

Brain-like intelligence is ushering humanity into an era of the Internet of Perceptions (IoP), where the vast amounts of data generated by numerous sensing nodes pose significant challenges to transmission bandwidth and computing hardware. A recently proposed near-sensor computing architecture offers an effective solution to reduce data processing delays and energy consumption. However, a pressing need remains for innovative hardware with multifunctional near-sensor image processing capabilities. In this work, Mott material (vanadium dioxide)-based photothermoelectric near-infrared photodetectors are developed that exhibit electrode-dependent and tunable super-linear photoresponse (exponent $\alpha > 33$) with ultralow modulation bias. These devices demonstrate an opto-thermo-electro-coupled phase transition, resulting in a large photocurrent on/off ratio (>10^5), high responsivity (≈500 A W^{-1}), and well detectivity (≈3.9 × 10^{12} Jones), all while maintaining rapid response speeds ($\tau_r = 2$ µs and $\tau_d = 5$ µs) under the bias of 1 V. This electrode-dependent super-linear response is found to arise from the electron doping effect determined by the polarity of the Seebeck coefficient. Furthermore, the work showcases intensity-selective near-sensor processing and night vision pattern reorganization, even with noisy inputs. This work paves the way for developing near-sensor devices with potential applications in medical image preprocessing, flexible electronics, and intelligent edge sensing.

1. Introduction

Optoelectronics have become integral to numerous aspects of our modern life, including optical communication, displays, smartphones, infrared detection and guidance, and medical diagnostics.[1–4] The demand for optoelectronic devices is exceptionally high in emerging areas, such as autonomous driving, artificial intelligence, and optical interconnection networks, which are pivotal for the future of 6G communication technology.[5–7] Of particular interest is the development of high-performance near-infrared (NIR) photodetectors for the C-band (1530–1565 nm), which has the lowest transmission loss in optical fibers and is widely used in optical communication.[8–11] These photodetectors must exhibit high sensitivity, low latency, and low power consumption. High sensitivity enhances the ability to detect ultra-low light intensities, which is crucial for good night vision performance. Low latency ensures immediate data transmission, which is vital for the safety and efficiency of motion detection systems.

B. Li, P. Xie, Y. Meng, W. Wang, B. Gao, Q. Quan, Y. Yan, M. Ding, J. C. Ho
Department of Materials Science and Engineering
City University of Hong Kong
Hong Kong SAR 999077, China
E-mail: johnnyho@cityu.edu.hk

B. Li
Shenzhen Research Institute of City University of Hong Kong
Shenzhen 518057, China

B. Chen, C. H. Chan
Department of Electrical Engineering
City University of Hong Kong
Hong Kong SAR 999077, China

B. Chen, C. H. Chan, J. C. Ho
State Key Laboratory of Terahertz and Millimeter Waves
City University of Hong Kong
Hong Kong SAR 999077, China

M. Yang, D. Li
Department of Physics
City University of Hong Kong
Hong Kong SAR 999077, China

J. C. Ho
Institute for Materials Chemistry and Engineering
Kyushu University
Fukuoka 816–8580, Japan

The ORCID identification number(s) for the author(s) of this article can be found under https://doi.org/10.1002/adma.202410952

DOI: 10.1002/adma.202410952

Moreover, to support the extensive and reliable information collection, Internet-of-Things facilities equipped with numerous NIR sensors need more energy-efficient sensing modules to address power consumption and heat dissipation challenges.[12–15] To improve the overall performance of NIR photodetectors, various approaches have been explored. For instance, Vandewal et al. focused on material modifications to achieve higher sensitivity,[16] while Wang et al. optimized structural design to enhance photoelectric conversion efficiency.[17] By employing the unipolar barrier concept, Kumar et al. achieved ultra-low dark current using Mott oxide,[18] and Chen et al. significantly improved the signal-to-noise ratio.[19] However, to the best of our knowledge, few studies have investigated the coupling relationship between electrode materials and the performance of photothermoelectric (PTE) NIR detectors, especially in conjunction with phase transitions in Mott oxides. This gap in research presents an exciting opportunity for further advancements in the field.

PTE detectors leverage the principles of photothermal conversion and the thermoelectric effect. Unlike conventional photodiodes or photomultiplier tubes, PTE detectors do not require a cooling unit or external bias, resulting in a relatively low sensing noise level and an improved signal-to-noise ratio.[20–22] These characteristics make them highly promising for self-powered light detection in space exploration, particularly in the NIR band, given the significant photothermal effect.[20,23–25] A strong candidate for this application is the light-field-induced metal-insulator transition (MIT) in quantum Mott oxides, such as vanadium oxide (VO_2). VO_2 exhibits a low threshold intensity and can be effectively regulated with a small bias voltage, providing a unique approach to achieving low-power NIR detection and a modulable super-linear photoresponse.[26–30] Nevertheless, for narrow-band VO_2-based two-terminal or heterogeneous photodetectors, it is challenging to suppress the dark current in either the insulating or metallic state due to high intrinsic conductance and the operative bias.[31–34] Alternatively, the inherent photothermoelectric effect between VO_2 and the metal electrode enables self-powered NIR detection without external bias.[35] During the phase transition, accompanied by a significant resistance change, the functional relationship of the photocurrent can transform from sub-linear to super-linear.[18,36–38] This transformation is critical for near-sensor vision processing and pattern classification, as it acts as an intensity selector, filtering out noise from the input pattern even with small variations in light intensity.[39,40] Despite these promising attributes, the effective utilization of the MIT in conjunction with the PTE effect of VO_2 to achieve ultra-low power consumption and super-linear photoresponse has not yet been demonstrated.

Herein, we developed a self-powered NIR ($\lambda = 1550$ nm) PTE detector with a simple metal-VO_2-metal structure on flexible mica. This device exhibits electrode- and power-dependent super-linear photoresponse under ambient conditions. Intriguingly, we discovered that the device's PTE-induced metal-insulator transition (MIT) strongly depends on the type of metal electrode used. The threshold intensity can be modulated with a small bias voltage ranging from 0 (self-powered) to 5 mV. Leveraging this opto-thermo-electro-coupled MIT effect, we achieved a transition from sub-linear to super-linear photoresponse in the Ni-electrode device as the NIR intensity increased from 0 (dark condition) to 4 nW μm^{-2}. This led to a maximum responsivity and detectivity up to 1 A W^{-1} and 10^{12} Jones, respectively. These results are attributed to the effective regulation of the Ni-electrode VO_2 detector with the PTE-induced phase transition, closely related to the electron doping effect influenced by the polarity of the electrode's Seebeck coefficient. Additionally, we present potential applications of our approach, including dynamic intensity separation and the classification of nocturnal patterns with noisy inputs. These findings lay the groundwork for developing high-performance photodetectors for various applications, including medical spectrometry, night vision, and smart edge sensors.

2. Results and Discussion

2.1. Device Structure and Characterization

The differences in the detector structure and electrode-dependent photoresponsiveness are illustrated in **Figure 1a**. In order to prepare the device, a thickness of ≈20 nm VO_2 film was epitaxially grown on the flexible mica substrate. The details of the growth are described in the Experimental Section. Given the significant dependence of MIT in the VO_2-based electronics on the quality of the channel material, X-ray diffraction (XRD), transmission electron microscopy (TEM), and related tools were used to evaluate the quality of VO_2 before characterizing the PTE-induced MIT phenomenon. First, the crystalline nature of the VO_2 film was measured by XRD. As shown in Figure 1b, a typical θ–2θ scan of the VO_2/mica heterostructure exhibits only the M-VO_2 (020) peak at 39.8° besides the mica (00l) series of peaks, demonstrating that the film was deposited without any impure crystalline phases or other orientations. Then, to address the fascinating feature of temperature-driven structural transformation between the M and R phases in VO_2, a variable-temperature Raman study was performed. Several A_g and B_g modes in Figure 1c show that the VO_2 film at room temperature (i.e., 25 °C) is of an insulating M phase with a space group of $P2_1/c$. Among these modes, 192, 223, 308, 389, and 498 cm^{-1} belong to the A_g symmetric pattern, while 264 and 338 cm^{-1} belong to the B_g symmetric pattern. The A_{1g} vibration pattern at 613 cm^{-1} is caused by the V-O stretching vibration. Raman peaks for other vanadium oxides did not appear, further confirming the high purity of our samples. As temperature increases to 80 °C, all these modes of M-VO_2 disappear, indicating the structural transition from the M to the R phase. The phonons of the R phase with a space group of D_{4h} are highly softened and damped.[41,42] On the other hand, to observe the effect of different metal electrodes on the phase transition behavior of VO_2 thin films, a variable-temperature resistance test was carried out. As depicted in Figure 1d, all the two-terminal VO_2 devices with various metal electrodes undergo a temperature-dependent MIT with a resistance change of three orders in magnitude around the T_c (i.e., 72 °C). These curves also exhibit a typical thermal hysteresis with a ≈10 °C width of the transition range, characteristic of a temperature-driven first-order phase transition. The transport results demonstrate that all the VO_2 PTE devices with different metal electrodes retain similar MIT behaviors, especially the value of T_c, which is a key factor in determining the critical light intensity for the PTE-induced phase transition.

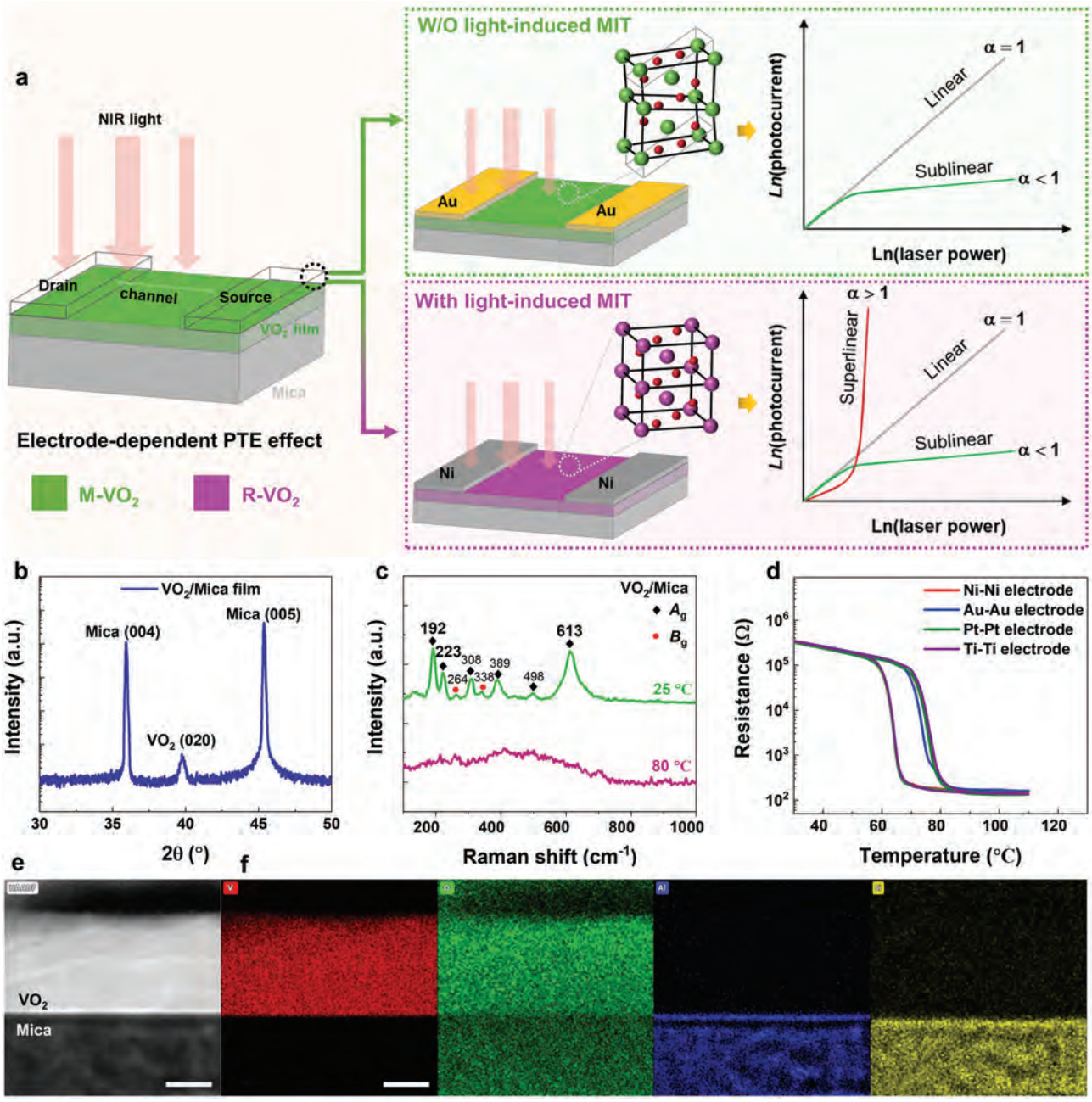

Figure 1. Device structure and characterization. a) Schematic diagram of the VO_2 PTE detector. The VO_2 film is epitaxially grown on a flexible mica substrate, with different metal materials selected as electrodes and deposited in the positions indicated by the transparent frame. When Au is selected as the electrode material, the VO_2 PTE detectors only show sub-linear and linear responsivity with $\alpha \leq 1$ (green dotted box). In contrast, when Ni is employed as the electrode, the VO_2 film layer can undergo the PTE-induced phase transition to produce super-linear photoresponsivity with $\alpha > 1$ (purple dotted box). In the device diagram, the green layer represents the monoclinic VO_2 crystalline phase (M-VO_2) as illustrated by the green vanadium atomic structure in the inset, and the purple layer represents the rutile VO_2 phase (R-VO_2) as depicted by the purple vanadium atomic structure. The width of the VO_2 channel is 20 μm. b) X-ray diffraction (XRD) pattern of the epitaxial VO_2 thin film on mica. c) Raman spectra of the epitaxial VO_2 film at temperatures of 25 and 80 °C. d) Typical R-T curves of the VO_2 PTE device with different electrode materials, including Ni, Au, Pt, and Ti. e,f) Cross-sectional HAADF-TEM image (e) and corresponding EDS maps (f) of the VO_2/mica heteroepitaxy. All scale bars are 10 nm.

To further examine the chemical state of the VO_2 film, the XPS curves are measured and compiled in Figure S1 (Supporting Information). The C *1s* level at 285 eV, shown in Figure S1a (Supporting Information), was used to calibrate the binding energy during the test. As shown in Figure S1b (Supporting Information), the doublet peaks for V *2p* can be observed at 515.2 and 516.3 eV, which are assigned to be the V^{3+} and V^{4+} states, respectively. The O *1s* level at 530.0 eV is associated with the vanadium oxide compound. The XPS results indicate that the epitaxial film is a VO_2 compound, as evidenced by

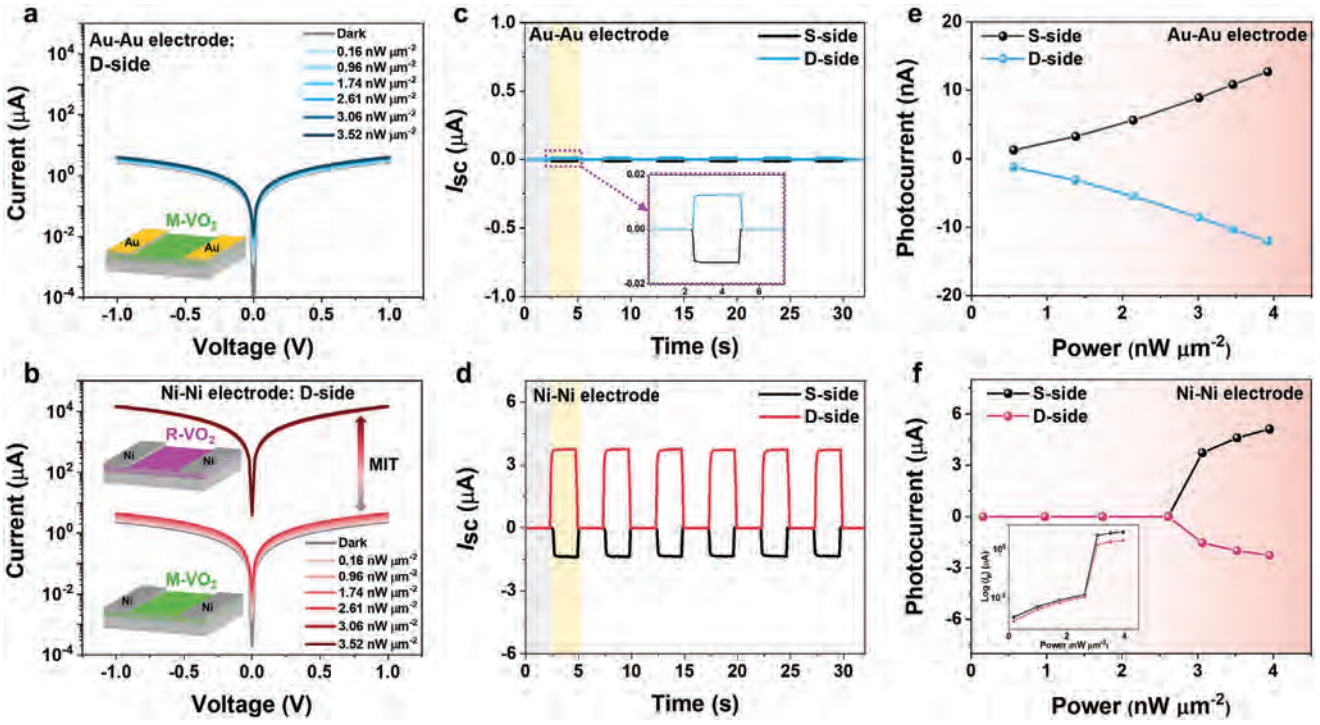

Figure 2. Electrode-dependent NIR photoresponse of the VO_2 PTE detectors. a,b) Room temperature *I–V* characteristics of Au- (a) and Ni- (b) electrode VO_2 photodetectors in the dark and under laser irradiation at varying power densities. Under the same irradiation conditions, only the Ni-electrode VO_2 photodetector undergoes the PTE-induced phase transition from monoclinic (green) to rutile (purple), as shown in the inset. c,d) Temporal response with the laser spot positioned on the drain VO_2/metal-electrode interface (D-side) and source interface (S-side) for the Au- (c) and Ni- (d) electrode VO_2 photodetectors. A magnified view of the panel (c) is shown in the purple dotted box. The yellow region represents laser on, and the gray region represents laser off. e,f) Dependence of photocurrent of the Au- (e) and Ni- (f) electrode VO_2 photodetectors on laser power. The inset shows the logarithmic graph of panel (f).

the energy difference (Δ≈13.7 eV) between the binding energy of the O *1s* level and V *2p*. However, some surface oxidation might have occurred. Furthermore, to obtain the crystal information at the interface of the VO_2/mica heteroepitaxy, transmission electron microscopy (TEM) was employed. Figure 1e shows the cross-sectional HAADF-TEM image of the heterogenous VO_2/mica interface, and Figure 1f corresponds to the EDS mapping for the main elements contained in the heterostructure. There is a sharp interfacial separation between the epitaxial VO_2 layer and the mica substrate, and the thickness of the VO_2 film is estimated to be ≈20 nm. The high-resolution TEM image of the enlarged VO_2/mica interface reveals the lattice fringes, indicating the VO_2 film is highly crystalline (Figure S2a, Supporting Information). The *d*-spacing of contiguous planes is ≈4.5 and 5.3 Å, corresponding to M-VO_2 (010) and mica (001) planes, respectively. Meanwhile, the selected area electron diffraction (SAED) pattern for the high-resolution TEM image is shown in Figure S2b (Supporting Information), which was labeled as the mica substrate in the [100] zone axis. With the SAED pattern, the epitaxial relationship between the VO_2 film and mica substrate can be confirmed as (010) VO_2 || (001) mica, consistent with the XRD and Raman results. These characterizations demonstrate that the VO_2 thin film grown on a mica substrate has high crystallinity without significant cracks or critical structural defects and is of a quality suitable for device applications.

2.2. Electrode-Dependent near-IR PTE Response

Figure 2a,b shows the room temperature *I–V* characteristics of the Au- and Ni-electrode VO_2 devices as a function of laser (1550 nm) intensity. As the power density increases from 0 to 3.52 nW μm^{-2}, the photocurrent of the Ni-electrode device increases by over three orders of magnitude. In contrast, the photocurrent of other devices, including the Au-, Pt-, and Ti-electrode ones, does not increase significantly under the same illumination conditions (Figure S4, Supporting Information). This difference in photocurrent likely originates from the PTE-induced MIT process, during which the positive PTE coupling efficiency between the Ni electrode and the VO_2/mica film facilitates the transport of hot electrons from the hot to the cold terminal, thereby aiding the electron-doping effect that assists the phase transition in the VO_2 channel.[43,44] Moreover, the photocurrent of the Ni-electrode device approaches saturation under 3.06 nW μm^{-2} illumination, indicating the threshold intensity required for the phase transition at zero bias. It is also known that the direction of PTE short-circuit current (I_{sc}) depends on the location of the illumination spot due to the Seebeck effect.[45,46] Therefore, the location-dependent I_{sc} of the Au- and Ni-electrode devices was measured under 3.06 nW μm^{-2} laser irradiation at zero bias. In Figure 2c,d, the I_{sc} of both the Au- and Ni-electrode devices is positive when the laser is shone on the drain (D) side but becomes negative when the laser is shone on the source (S) side, demonstrating

an apparent PTE characteristic. However, the maximum I_{sc} value for the Ni-electrode device reaches up to 4 μA (Figure 2d), compared to ≈10 nA for other VO_2 devices with different metal electrodes (Figure 2c; Figure S5, Supporting Information). The significant difference in the I_{sc} value further confirms that the PTE-induced MIT is triggered only in the Ni-electrode device under the same conditions. Additionally, as shown in Figure S9 (Supporting Information), the PTE-induced MIT effects in the Au- and Ni-electrode photodetectors were characterized by an in situ Raman measurement. It demonstrates that only the Ni-electrode device exhibits PTE-induced MIT behavior under the same NIR light illumination conditions.

Furthermore, the photocurrent and photovoltage of the Au- and Ni-electrode detectors are presented as a function of power density in Figure 2e,f, and Figure S6 (Supporting Information), respectively. As shown in Figure 2e, as the optical power increases from 0.16 to 3.95 nW μm^{-2}, the photocurrent of the Au-electrode device increases gradually without any abrupt changes, including on both D and S sides. In contrast, as the radiation power increases, the photocurrent of the Ni-electrode device increases significantly from a few nanoamps to microamps, with a sharp rise when the power exceeds 2.61 nW μm^{-2} (Figure 2f). This is consistent with the results in Figure 2b and further demonstrates that the MIT process occurs only in the Ni-electrode device. Similarly, the photovoltage generated by a self-powered VO_2-based photodetector serves as another indicator to verify the PTE effect. As shown in Figure S6 (Supporting Information), all PTE detectors exhibit increasing photovoltage with rising laser power. However, the Ni-electrode detector shows a cliff-like attenuation near the phase-change threshold intensity. This can be explained by the sudden decrease in the Seebeck coefficient of the VO_2 film during the MIT process, which sharply weakens the PTE coupling efficiency, as illustrated in Figure 4g,i.[52] These results confirm that the NIR photoresponse of our devices is electrode-dependent, with the Ni-electrode device producing stronger PTE coupling with VO_2 to induce the phase transition, thereby enhancing the NIR response. It is noted that the ohmic contact formation was confirmed with different electrodes on all the VO_2 devices to exclude the effects of the Schottky junction on the device characteristics discussed above (Figure S3, Supporting Information).

2.3. Dynamic near-IR Photoresponse Characteristics

To measure the dynamic photo-sensing properties, the device's transient photoresponse (photocurrent-time, I_p-t) was tested with different applied biases starting from 0 to 5 mV. The I_p-t response to varying applied biases and irradiation power density (P) is shown in the various panels of **Figure 3a**. According to Figure 3a, it is evident that the device displays an obvious photoresponse that regulates significantly with increasing the applied biases and/or NIR intensity. For instance, the I_p was modest (≈1 μA) for 0 mV and 2.8 nW μm^{-2} (see panel (ii) in Figure 3a), whereas I_p enhances to ≈10 μA with increasing the operative voltage to 5 mV, despite maintaining the same P (i.e., 2.8 nW μm^{-2}). Similarly, an increase in the light intensity results in an increase in the I_p with a bias voltage of 5 mV (i.e., the reduced intensity threshold of MIT), which indicates that the I_p generation is driven by the photo-absorbance-induced gradient in carrier concentration or energy (see panels (viii) to (ix) in Figure 3a). The current enhancement ratio (i.e., $E = (\frac{I_5 - I_0}{I_0}) \times 100\%$, where I_5 and I_0 are the I_p values at 5 and 0 mV) with an intensity of 2.6 nW μm^{-2} was calculated to 3.11×10^3%. This essential enhancement provides further evidence that MIT can produce a strong modification of the device's light response.

As the response time is one of the main characteristics of the photodetector, the rise time (τ_r, i.e., time taken for I_p to reach 90% of its maximum value) and decay time (τ_d, i.e., time taken for I_p to fall from maximum to 10%) is calculated. Intriguingly, the response times also exhibit electrode-dependent characteristics of the devices. For instance, the Au-electrode device showed a slow response (τ_r = 2.7 ms and τ_d = 1.6 ms) at 0 mV and P = 3.8 nW μm^{-2} (Figure 3b). In contrast, a fast photoresponse (τ_r = 0.18 ms and τ_d = 0.17 ms) was observed for the Ni-electrode device under the same operating conditions (Figure 3c). If the bias is further increased to enhance carrier separation, the Ni-electrode device can demonstrate even higher response speeds (τ_r = 2 μs and τ_d = 5 μs), as shown in Figure S10b (Supporting Information). Furthermore, the response time dependency on the metal electrode types is depicted in Figure 3d and Figure S7 (Supporting Information). Notably, the Ni-electrode device shows a decrease of up to one order of magnitude in the response time. At the same time, other types of electrodes exhibit similar rise and decay times under the self-powered mode, indicating a distinct electrode-dependent high-speed operation. According to the Seebeck effect, the slow response time with Pt, Ti, or Au electrode is caused by their positive Seebeck coefficients, which prevent charge carriers generated by laser irradiation from being injected into the VO_2 channel to induce the opto-thermo-electro-coupled phase transition. On the contrary, the fast photoresponse can be attributed to the negative Seebeck coefficient of the Ni electrode on the VO_2 device, which not only helps to separate the electron-hole pairs but also effectively enhances the injection of electrons into the VO_2 layer, thus significantly reducing the light intensity threshold for MIT. A more detailed analysis is provided in the mechanism explanations below.

On the other hand, to obtain the noise current, we performed the Fourier transform of the dark current versus time. In general, shot noise (i_{shot}), thermal noise ($i_{thermal}$), generation recombination noise ($i_{g\text{-}r}$), and 1/f noise ($i_{1/f}$) can contribute to a semiconductor-based photodetector, which leads to the overall noise of $i_{noise} = [i_{shot}^2 + i_{thermal}^2 + i_{g-r}^2 + i_{1/f}^2]$, where $i_{shot} = \sqrt{2eI_{dark}\Delta B}$, $i_{thermal} = \sqrt{4k_B T \Delta B / R}$, $i_{g-r} = i(f, B)_{g-r}$, and $i_{1/f} = i(f, B)_{1/f}^2$, where e is the charge of an electron, k_B is the Boltzmann constant, T is the absolute temperature, ΔB is the bandwidth in hertz, R is the shunt resistance of the device, and f is the frequency.[47–49] Particularly, for the PTE detectors, no external bias is required, and 1/f noise can be ignored, so the dominant noise here is mostly the shot and thermal noise. The calculated i_{noise} corresponding to different frequencies is shown in Figure S8 (Supporting Information). It should be noted that the average i_{noise} is dominated by $i_{shot} + i_{thermal}$ at frequencies higher than 0.1 Hz, independent of the frequency. It is observed that the noise of both the Au- and Ni- electrode devices are ≈4.0×10^{-14} A Hz$^{-1/2}$ under 5 mV, is frequency-independent, and is close to the calculated i_{shot} value using the dark current with peaks

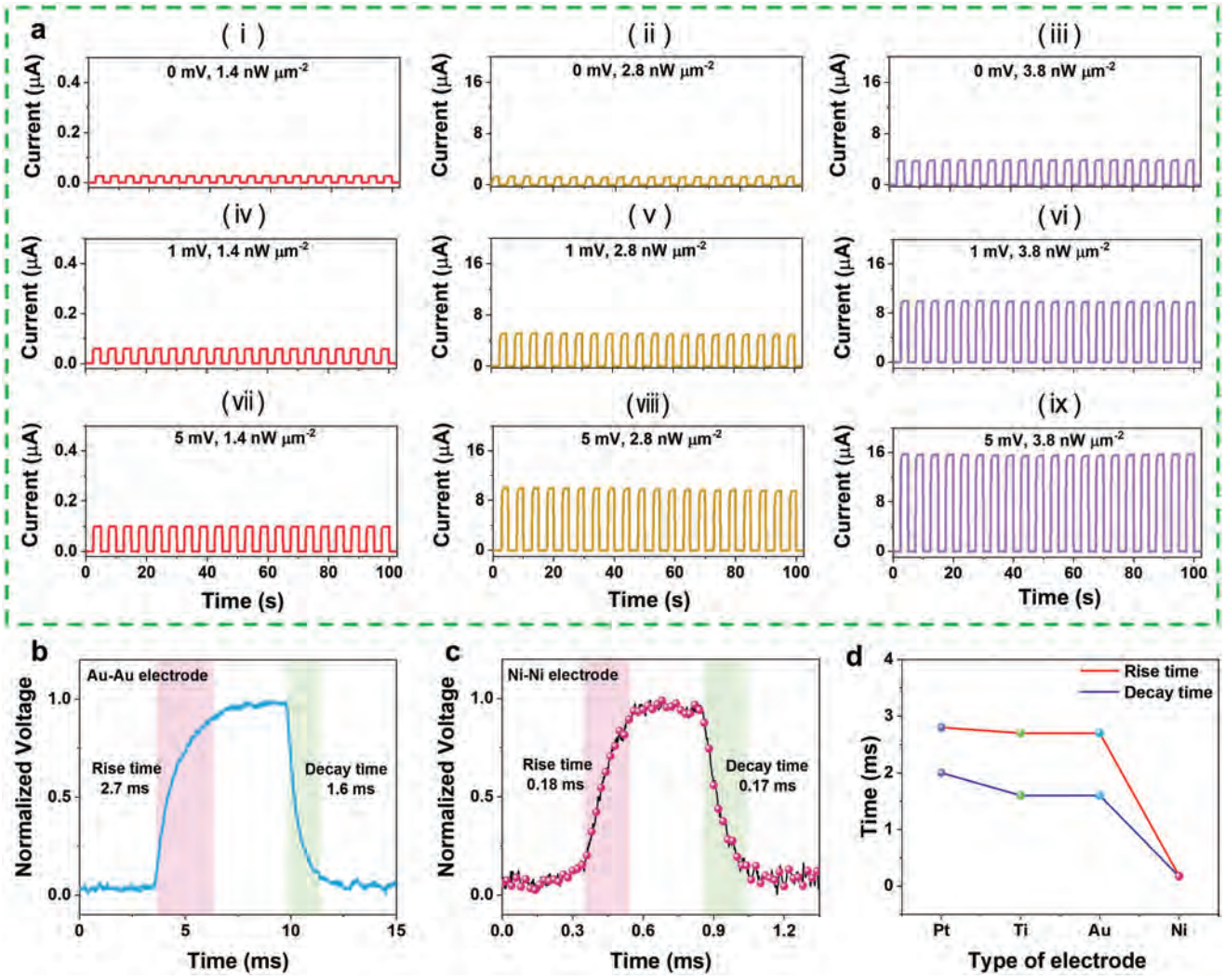

Figure 3. Dynamic near-IR photoresponse. a) Time-dependent photoresponse collected with different operating biases and irradiating intensities. The values of the applied bias and irradiating intensity are shown in the respective panels in order of (i) to (ix). The Ni-Ni electrode was used for this performance test under 1550-nm laser irradiation. b,c) The rise and decay times of the VO_2 PTE detectors with the Au- (b) and Ni- (c) electrode material, respectively. The Ni-electrode VO_2 PTE detector shows response times faster by about one order of magnitude than the Au-electrode detector. d) Corresponding statistical results of the electrode-dependent response times of the VO_2 PTE detectors with the radiation power of 3.8 nW μm^{-2} at 0 mV.

originating from environmental sources.[47,48] Since the i_{shot} is related to the leakage current, the relatively low i_{noise} indicates suppression of leakage current, benefiting from the high quality of the VO_2 film with fewer traps, as characterized by the TEM in Figure 1 and Figure S2 (Supporting Information).

2.4. Electrode-Dependent Sub-to-Super-Linear Photoresponsivity and Mechanism

To explore the difference in electrode-dependent photoresponse coefficient (α), where the value of the exponent ($\alpha = d\ln(I_p)/d\ln(P)$) relies on the magnitude of the irradiation intensity. The photocurrent on/off ratio (i.e., I_p/I_{dark}) for Au- and Ni-electrode VO_2 PTE detectors was calculated as a function of power density for three specific (but not limited) applied drain biases (V_d), including 0, 1, and 5 mV. It is worth noting that the I_p on/off ratio of both Au- and Ni-electrode devices is strongly dependent on the applied bias and P values. In particular, the Au-electrode device shows an I_p on/off ratio close to 4.0 for p = 0.16 nW μm^{-2} and 0 mV, whereas it only enhances to 45.9 even with increasing the P to 3.95 nW μm^{-2}, as shown in **Figure** 4a. However, the on/off ratio for the Ni-electrode device greatly enhances to 1.1×10^4 with increasing the P to 3.95 nW μm^{-2}, as depicted in Figure 4b. More importantly, the I_p on/off ratio follows the power law (i.e., P^{α}), where the value of α depends on the magnitude of the irradiation intensity. With an applied bias of 5 mV, the α value for the Au-electrode device was measured to 0.32 (i.e., <1) until the P increased to 3.95 nW μm^{-2}, indicating the sub-linear behavior.[18,39] In contrast, the on/off ratio of the Ni-electrode device increases rapidly. It reaches a value of $\alpha = 26$ with increasing the p values, leading to a shift in the photocurrent

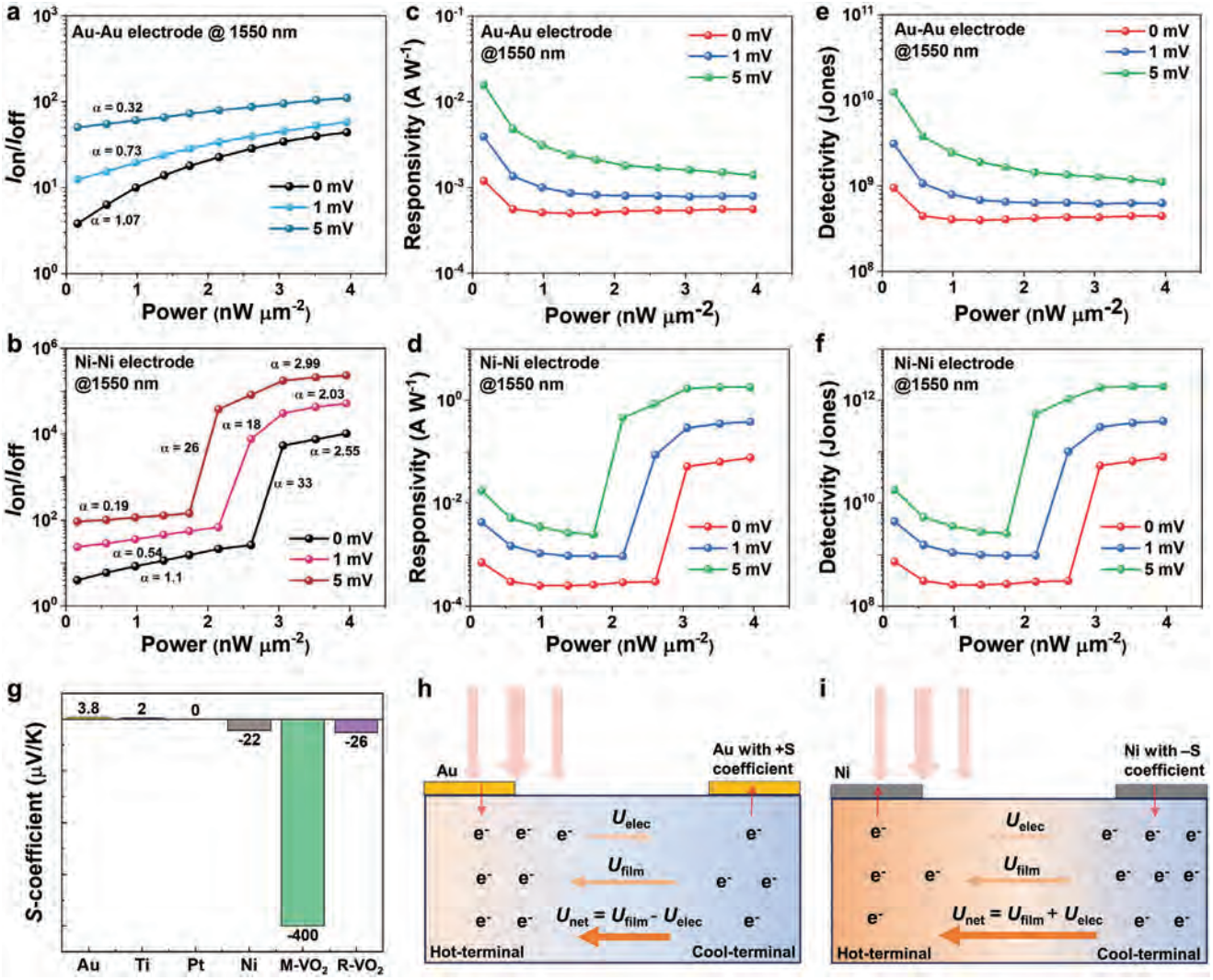

Figure 4. Near-IR photoresponse parameters. a,b) The photocurrent on/off ratio as a function of irradiating intensities for Au- and Ni-electrode VO_2 PTE detectors with three different applied biases of 0, 1, and 5 mV plotted on a logarithmic scale. The curves were fitted with a power law, and the fitting exponent is shown in the respective panels. c,d) Corresponding calculated responsivity for Au- and Ni-electrode VO_2 PTE detectors at three different applied biases. e,f) Corresponding calculated detectivity for Au- and Ni-electrode VO_2 PTE detectors at three different applied biases. g) The Seebeck coefficients of different metal electrodes and VO_2 film in a monoclinic or rutile state. h,i) Schematic diagrams of electrode-dependent electron diffusion paths across the channel under light irradiation. The net potential (U_{net}) is equal to the PTE potential of the VO_2 film (U_{film}) minus (h) or plus (i) the PTE potential from the electrode (U_{elec}). The blue color represents the M-VO_2, and the orange color is the R-VO_2. "Hot-terminal" denotes the drain region, and "Cool-terminal" is the source region. Here, the left direction is specified as the positive direction of the potential.

behavior from sub- to super-linear, as shown in Figure 4b. These results have remarkable implications for low-power near-sensor processing applications, as our device achieves sub-to-super-linear photoresponses with ultralow operative voltages in a single device, representing a significant technological advance.

Furthermore, other standard figures-of-merit for photodetectors include photoresponsivity (R) and detectivity (D^*), which quantify the device's capacity to the minimum detectable light intensity.[18,48,50] Mathematically, R is defined as $R = I_p/(P \cdot S)$, where S is the effective irradiation area (6×10^{-3} mm^2) and $D^* = R \cdot \sqrt{S/2eI_{dark}}$, where e is the elementary charge (i.e., 1.6×10^{-19} C). The calculated R and D^* values as a function of light intensity are depicted in Figure 4c–f, respectively. Specifically, with an applied bias of 5 mV, the maximum R and D^* values for the Au-electrode device were only close to 1.6×10^{-2} A W^{-1} and 1.3×10^{10} Jones, and continued to decrease as the light intensity increased. On the other hand, an R value of 1.95 A W^{-1} and D^* value up to 2.01×10^{12} Jones were measured for the Ni-electrode device, which is two orders of magnitude better than the former. Further, a higher R value of 500 A W^{-1} and D^* value up to 3.9×10^{12} Jones were achieved by applying a bias of 1 V (Figure S10a, Supporting Information). The comparison in Figure S11 (Supporting Information) shows the VO_2 PTE detector shows outstanding NIR detection performance compared with previous reports (Table S2, Supporting Information). Such high responsivity and speed allow for more accurate detection of the input

optical signals. The device's performance could be further enhanced by designing special metasurface and electrode structures,[45,51] which can improve the opto-thermo-electric coupled efficiency and photon-absorbing area. Importantly, the key behind the sub-to-super-linear photoresponse transition is the MIT; however, the device operates like a conventional junction before and after the MIT and thus shows sub- or near-linear response in those ranges.

The Seebeck coefficient of a material, also known as the thermoelectric potential, is expressed in S and represents the voltage of the thermoelectric potential generated by the material for a given temperature difference.[20,22] In this case, one can define $|S| = \Delta U/\Delta T$, where ΔU represents the potential difference and ΔT represents the temperature difference. It is worth noting that for most thermoelectric materials, the sign of S determines the flow of internal net carriers (i.e., the direction of the thermoelectric potential). That means when S is negative, the transport of electrons is mainly from the hot end to the cold end; conversely, when S is positive, the transport of electrons is mainly from the cold end to the hot end. To explain the electrode-dependent PTE-induced MIT behavior, we compare the S values of different metal film electrodes as shown in Figure 4g. It is evident that both the S-coefficients of M-VO_2 and Ni-electrode film are negative (i.e., −400 and −22 μV K^{-1}),[52,53] and the thermoelectric potentials generated by them have the same direction. This promotes the drift and aggregation of electrons from the hot to the cold terminal, as depicted in Figure 4i. The electron doping effect greatly reduces the phase transition barrier of VO_2 (i.e., the intensity threshold), resulting in a Mott-activated super-linear photoresponse. In contrast, as depicted in Figure 4h, the metal electrode with a positive S coefficient has the opposite direction of thermoelectric potential compared with the VO_2 film material.[54,55] Consequently, electrode-assisted electron doping on the VO_2 layer cannot occur to reduce the intensity threshold of MIT at 1550 nm. To sum up, the polarity of S determines the electron doping effect of the metal electrode on the VO_2 layer and subsequently affects the photoresponsivity of the VO_2 PTE device.

2.5. Near-Sensor Imaging Applications

As mentioned above, the near-sensor computing architecture, which involves moving the sensing and computing parts to the edge sensors, could reduce unnecessary data transmission. This offers a promising model for significantly reducing data processing latency and power consumption. As two potential applications based on the VO_2 PTE sensor, we implement near-sensor image processing for dynamic intensity separation and night pattern classification to enhance overall efficiency by executing processing close to the sensor and eliminating noisy backgrounds. Specifically, this method removes noise signals, typically characterized by lower light intensity than the key features, while amplifying the signals corresponding to the key features near the photodetector. This process eliminates unnecessary data and improves vision accuracy. The ability to provide an intensity-selective, tunable sub-to-super-linear photoresponse is crucial for effective near-sensor processing. Notably, our device exhibits a self-powered, opto-thermo-electro-coupled photoresponse, making it an ideal low-power platform for near-sensor image processing. As demonstrated by the reproducible photoresponse in Figure 3, the device shows highly stable flipping under both voltage and/or light irradiation.

To perform the near-sensor processing, the photosensor was initially scanned in the X_2-Y_2 plane perpendicular to the Z-direction of stationary laser irradiation without the mask, as shown schematically in **Figure 5**a. It is noted that the spot intensity changes in the x-y plane, as depicted in Figure 5b, which could be attributed to the diffraction effect of the resonator in the laser used. Furthermore, to confirm the threshold photo-sensing nature depending on the operative biases, the photocurrent (I_p) was tested by fixing the sensor at three distinct locations (indicated by the colored dots in Figure 5b), which correspond to the different light intensities of 0.16, 2.7, and 3.9 nW μm^{-2} and data was collected with voltages applied in incremental steps, as shown by the voltage curve in Figure 5c. Especially, the device generates a photocurrent that depends on both the intensity and the applied voltage. This unique feature allows the device to adapt to varying light conditions and adjust its processing power accordingly. For instance, Figure 5c shows that for intensities higher than 2.7 nW m^{-2}, the device operates with decremental operating voltages from 5 to 0 mV (green curve in the bottom panel). This ability to operate with lower voltages implies that the device can be more energy-efficient, which is a significant advantage in applications where power consumption is a concern. On the contrary, for intensities lower than 2.7 nW μm^{-2}, the I_p is nominal (i.e., nA) for an operating voltage of 0 mV (see blue and yellow curves), allowing the intensities to be selected. This finding is important because the VO_2 device can not only act as a photosensor but also as a processing unit to execute near-sensor processing with lower operative voltages in the conventional bands of optical communication.

For the image-scale near-sensor processing, the laser was irradiating with two mixed patterns, i.e., the letter "C" and "U"; however, both have various intensities. In particular, the letter "C" was irradiating with an intensity of 1.4 nW μm^{-2}, whereas the intensity corresponding to the letter "U" was 2.8 nW μm^{-2}, as shown in Figure 5d. The details of the measurement are shown in Figure 5a. The laser and VO_2 photodetector were aligned along the Z-axis, and the mask in between was shifted in the X_1-Y_1 plane with a step of 6 mm. Then, the I_p was measured for each pixel with an operative voltage of 0 mV. As shown in the I_p map (Figure 5e) and colored line profile corresponding to the dotted lines in Figure 5f,g, the letter "U" (i.e., for higher intensity) was identified in the I_p map. In contrast, the letter "C" did not show any notable brightness, resulting in the recognizable input patterns.

Also, the device is capable of removing unwanted noise while remaining passive. To evaluate this capability, the device was subjected to rigorous testing for extremely high noisy inputs. For example, noise singles exceeding 80% of the key feature were added to different pixels, and photocurrent I_p was mapped with various operative voltages. As illustrated in Figures 5h,i, two distinct masks in the shapes of letters "C" and "Z" were utilized and divided into 6 × 6 pixels. Following each shifting, voltage bias in the shape of the step was applied, and the photocurrent was measured. It is noteworthy that, contingent on the operative bias, the I_p maps of the letter "C" corresponding to the noise

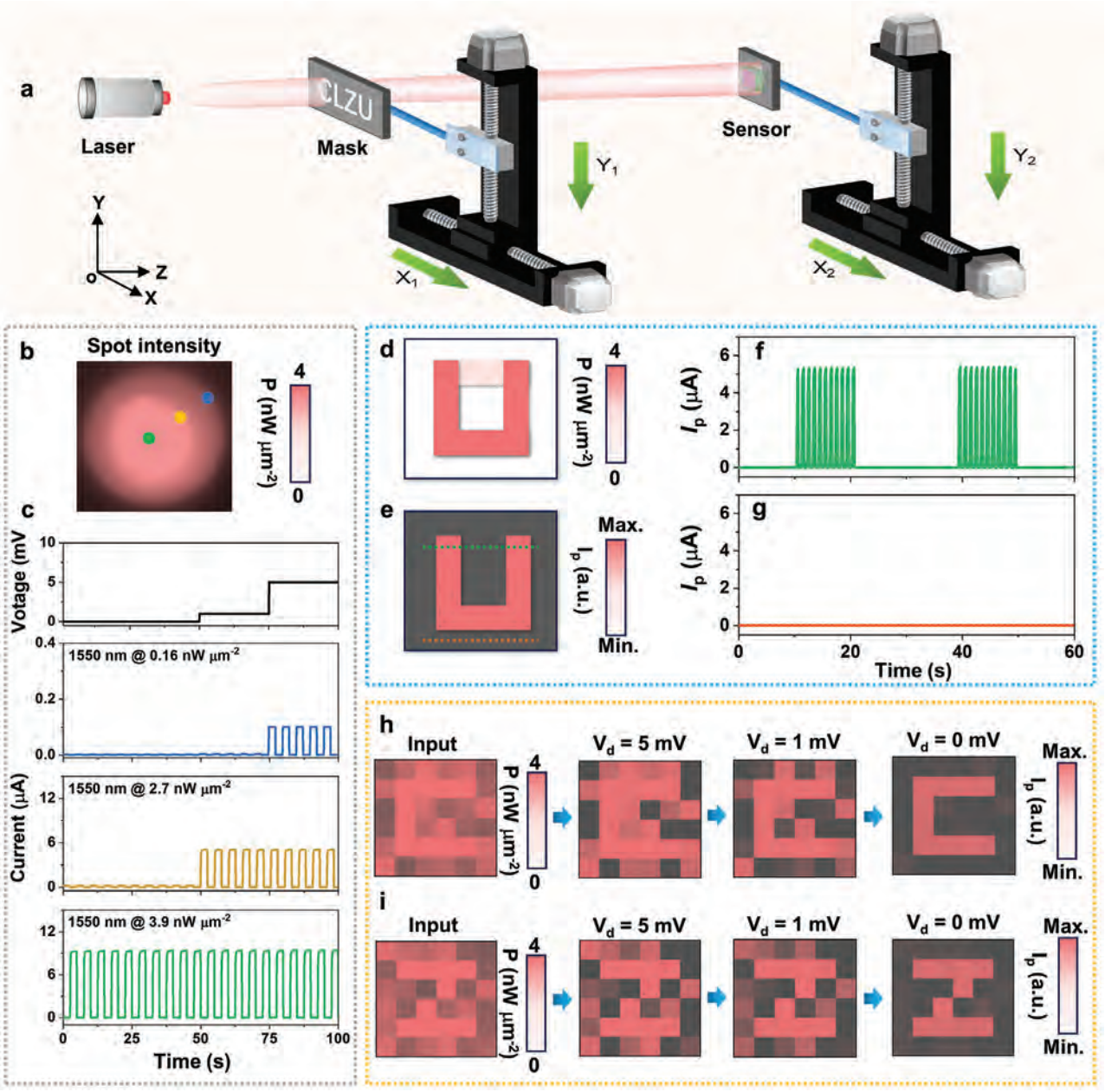

Figure 5. Near-sensor image processing. a) Schematic diagram of the near-sensor processing light system. To examine the adaptive-imaging ability, the sensor and masks in the shape of letters "C," "Z," and "U" were scanned procedurally in the x-y plane at different operative voltages. b) The measured intensity distribution in the x-y plane, which exhibits an approximate Gaussian distribution as illustrated by the pink light column in (a). c) Steps of the applied bias V_d (black curve) and measured photocurrent at fixed locations (indicated by colored dots in (b)) are shown by the blue, yellow, and green curves from the top to bottom panels, respectively. For pattern recognition, the 1550-nm laser and photosensor were fixed, and masks with different patterns were scanned in the x-y plane. d,e) Input intensity with letters "C" and "U" (d), where "U" is the key feature and "C" is the unwanted noise signal. The mapped photocurrent with operative bias $V_d = 0$ V, shows clear vision for the letter "U" (e). f,g) The measured photocurrent line profiles for the dotted green and orange lines on (e) are shown in figures (f) and (g), respectively. h,i) Input patterns "C" (h) and "Z" (i) with extremely high levels of noise and the measured current maps with different biases applied in sequential current maps.

input become undetectable at lower intensities and ultimately almost cease to exist, as illustrated in the sequential I_p maps in Figure 5h. Instead, the signal for the key object is visible, as shown in Figure 5h. Similarly, the device was tested with the letter "Z" pattern, and the resulting I_p mappings for different operative voltages are shown in the sequential images in Figure 5i. This was done to ensure that the device could correctly classify the input patterns.

As detailed in Table S1 (Supporting Information), the assessment of intelligent edge sensors typically encompasses three primary technical parameters: power consumption, integration density, and response speed.[39,40] Regarding power

consumption, the VO_2 PTE device leverages self-powered NIR detection capabilities based on the PTE effect. It also demonstrates a tunable sub-to-super-linear photoresponsivity with an ultralow modulation bias from 0 to 5 mV, representing a substantial reduction compared to previously reported results.[18,36,56] Regarding integration density, the VO_2 detector is manufactured using standard micro-nanofabrication techniques, such as sputtering, photolithography, etching, etc. This fabrication scheme aligns seamlessly with commercial CMOS processes, facilitating cost-effective large-scale array production. Furthermore, the VO_2 PTE detector features regulable sub-to-super-linear responsivity for near-sensor processing and night vision pattern reorganization, enabling higher-density integration of edge sensors from a multifunctional standpoint. Moreover, in the response speed, the VO_2 sensor achieves microsecond-level responsiveness. While this may not be considered rapid relative to the latest commercial product shown in Table S2 (Supporting Information), it has already surpassed prevailing commercial flash memory read/write speeds (in milliseconds), offering the potential to mitigate edge sensing and processing delays.

3. Conclusion

In summary, the integrative metal-VO_2-metal NIR photodetectors were created and demonstrated with self-powered photodetection and tunable super-linear photoresponsivity by utilizing the PTE properties of VO_2. Particularly, the device shows PTE-induced MIT, which is highly dependent on the type of metal electrode, and the threshold intensity can be modulated with a small bias from 0 (i.e., self-powered) to 5 mV. Based on this opto-thermo-electronic coupled MIT effect, sub-to-super-linear photoresponses were achieved in the Ni-electrode device by increasing the NIR intensity from 0 (i.e., dark condition) to 4 nW μm^{-2} with a microsecond range of response time and an on/off ratio of up to 10^5, leading to a maximum responsivity and detectivity up to 500 A W^{-1} and 3.9×10^{12} Jones, respectively. The effective modulation of the Ni-electrode VO_2 detector through the PTE-induced phase transition is believed to be responsible for these outcomes. We also found an electrode-dependent electron doping effect influenced by the polarity of the electrode's Seebeck coefficient, which determines the intensity threshold of MIT to induce the super-linear photoresponse. In addition, dynamic intensity separation and classifying nocturnal patterns with noisy inputs are presented as potential applications of our strategy. These findings will lay the groundwork for creating high-performance photodetectors for a broad range of applications, like intelligent edge sensing, night vision, and medical image preprocessing.

4. Experimental Section

Film Growth and Device Fabrication: High-quality monoclinic VO_2 films were epitaxially deposited on the artificially cleaved fresh mica (001) substrate by an rf-plasma-enhanced reactive magnetron sputtering system with a base vacuum pressure better than 1×10^{-7} Torr. During the growth, the substrate temperature and sputtering power were set at 500 °C and 100 W with an argon-oxygen flow ratio of 10:1 at a pressure of 3 mTorr. The growth thickness and rate were monitored by a crystal oscillator (SQC-310, INFICON). Then, the VO_2/mica devices were fabricated using the standard wet-etching process with the phosphoric acid solution. After that, the position of electrode patterns was defined by UV lithography and then exposed to the phosphoric acid etching solution, while the VO_2 channel was protected by a photolithography-patterned photoresist. Finally, different metals, including Ni, Au, Pt, and Ti layers, were selected as electrode materials and deposited on VO_2 by electron beam and thermal evaporations with a base pressure of 2×10^{-6} Torr and a deposition rate of 1 Å s^{-1}, followed by the standard lift-off process.

PTE Performance Measurements: Photodetectors were excited by a 1550 nm (near-infrared) laser through an objective lens (10×, NA = 0.7) and were calibrated by a power meter (PM400, Thorlabs). Time-, spatial-, bias-, and power-dependent photocurrent were measured by a commercial semiconductor analyzer (B1500A, Keysight) attached to a Lake Shore probe station. The position of the spot and VO_2 sensor was controlled by a programmable three-axis shifter on a standard optical platform. The photoswitching test was performed with an electrical chopper (AFG-2005, GWINSTEK). The modulation time-dependent measurement was carried out by Stanford Research SR-570 low-noise preamplifier with Textronix TBS1102B oscilloscope.

Other Physical and Chemical Characterizations: The crystal structure of VO_2 films was characterized by an X-ray Diffractometer (SmartLab 9 kW, Rigaku) with Cu Kα radiation (λ = 1.54178Å). Raman spectra were performed by the WITec Alpha 300R Raman system equipped with a variable-temperature station and an excitation wavelength of 532 nm. The temperature-dependent resistance curve was acquired on a commercial electrotransport test system (MPS-PTH, NEXTRON) with the four-probe principle. High-resolution transmission electron microscopy (JEM ARM-300F) analysis was conducted to obtain the cross-sectional image of the device with the operation voltage of 200 kV. The sample was sliced by a focused ion beam (FEI, Helios NanoLab650) with a C passivation layer for the TEM analysis. The distribution of elements was obtained from the EDS mapping in our materials.

Supporting Information

Supporting Information is available from the Wiley Online Library or from the author.

Conflict of Interest

The authors declare no conflict of interest.

Author Contributions

B.L., P.X., and B.C. contributed equally to this work. B.W.L. and J.C.H. conceived and designed the research. B.W.L. prepared materials, fabricated devices, and performed all characterization analyses. B.J.C. and C.H.C. performed device array fabrication. P.S.X., Y.M., and W.J.W. performed photoelectric characterization. M.W.Y. and D.F.L. performed the XRD measurement and analysis. B.X.G., Q.Q., Y.Y., and M.Q.D. helped with device fabrication and electrical characterizations. B.W.L., P.S.X., D.F.L., C.H.C., and J.C.H. wrote the related discussions. All authors discussed the results and commented on the manuscript.

Data Availability Statement

The data that support the findings of this study are available from the corresponding author upon reasonable request.

Keywords

near-infrared photodetector, near-sensor processing, phase transition, super-linear

Received: July 26, 2024
Revised: October 1, 2024
Published online:

[1] J. Shi, J. Zhang, L. Yang, M. Qu, D. C. Qi, K. H. L. Zhang, *Adv. Mater.* **2021**, *33*, 2006230.
[2] F. Wang, K. Pei, Y. Li, H. Li, T. Zhai, *Adv. Mater.* **2021**, *33*, 2005303.
[3] S. Chang, J. H. Koo, J. Yoo, M. S. Kim, M. K. Choi, D. H. Kim, Y. M. Song, *Chem. Rev.* **2024**, *124*, 768.
[4] S. Yuan, C. Ma, E. Fetaya, T. Mueller, D. Naveh, F. Zhang, F. Xia, *Science* **2023**, *379*, eade1220.
[5] N. Chi, Y. J. Zhou, Y. R. Wei, F. C. Hu, *IEEE Veh. Technol. Mag.* **2020**, *15*, 93.
[6] X. P. Ou, Y. Qiu, M. Luo, J. J. Li, X. B. He, J. F. Gao, F. J. Sun, P. Zhang, G. Yang, A. Y. Du, B. Li, Z. C. Liu, Z. H. Li, L. Xie, X. Xiao, J. Luo, W. W. Wang, J. Tao, Y. Yang, *Adv. Mater. Technol.* **2024**, *9*, 2300998.
[7] K. He, C. Wang, Y. He, J. Su, X. Chen, *Chem. Rev.* **2023**, *123*, 13796.
[8] T. He, H. Ma, Z. Wang, Q. Li, S. N. Liu, S. K. Duan, T. F. Xu, J. C. Wang, H. T. Wu, F. Zhong, Y. T. Ye, J. H. Wu, S. Lin, K. Zhang, P. Martyniuk, A. Rogalski, P. Wang, L. Li, H. T. Lin, W. D. Hu, *Nat. Photonics* **2024**, *18*, 60.
[9] L. Seravalli, *Microelectron. Eng.* **2023**, *276*, 111996.
[10] Y. Yu, S. Liu, C. M. Lee, P. Michler, S. Reitzenstein, K. Srinivasan, E. Waks, J. Liu, *Nat. Nanotechnol.* **2023**, *18*, 1389.
[11] G. L. Whitworth, M. Dalmases, N. Taghipour, G. Konstantatos, *Nat. Photonics* **2021**, *15*, 738.
[12] Q. F. Shi, B. W. Dong, T. Y. Y. He, Z. D. Sun, J. X. Zhu, Z. X. Zhang, C. Lee, *InfoMat* **2020**, *2*, 1131.
[13] L. L. Li, D. P. Wang, D. Zhang, W. H. Ran, Y. X. Yan, Z. X. Li, L. L. Wang, G. Z. Shen, *Adv. Funct. Mater.* **2021**, *31*, 2104782.
[14] S. Lee, R. Peng, C. Wu, M. Li, *Nat. Commun.* **2022**, *13*, 1485.
[15] M. A. Jamshed, K. Ali, Q. H. Abbasi, M. A. Imran, M. Ur-Rehman, *IEEE Sens. J.* **2022**, *22*, 5482.
[16] Q. Liu, S. Zeiske, X. Jiang, D. Desta, S. Mertens, S. Gielen, R. Shanivarasanthe, H. G. Boyen, A. Armin, K. Vandewal, *Nat. Commun.* **2022**, *13*, 5194.
[17] Y. Dai, X. Wang, W. Peng, C. Xu, C. Wu, K. Dong, R. Liu, Z. L. Wang, *Adv. Mater.* **2018**, *30*, 1705893.
[18] M. Kumar, S. Lim, J. Kim, H. Seo, *Adv. Mater.* **2023**, *35*, 2210907.
[19] Y. Chen, Y. Wang, Z. Wang, Y. Gu, Y. Ye, X. Chai, J. Ye, Y. Chen, R. Xie, Y. Zhou, Z. Hu, Q. Li, L. Zhang, F. Wang, P. Wang, J. Miao, J. Wang, X. Chen, W. Lu, P. Zhou, W. Hu, *Nat. Electron.* **2021**, *4*, 357.
[20] X. Lu, L. Sun, P. Jiang, X. Bao, *Adv. Mater.* **2019**, *31*, 1902044.
[21] M. J. Dai, X. R. Zhang, Q. J. Wang, *Adv. Funct. Mater.* **2024**, *34*, 2312872.
[22] F. H. Koppens, T. Mueller, P. Avouris, A. C. Ferrari, M. S. Vitiello, M. Polini, *Nat. Nanotechnol.* **2014**, *9*, 780.
[23] Y. J. Zhong, L. Zhang, V. Linseis, B. Qin, W. D. Chen, L. D. Zhao, H. W. Zhu, *Nano Energy* **2020**, *72*, 104742.
[24] K. Yoshioka, T. Wakamura, M. Hashisaka, K. Watanabe, T. Taniguchi, N. Kumada, *Nat. Photonics* **2022**, *16*, 718.
[25] X. Cai, A. B. Sushkov, R. J. Suess, M. M. Jadidi, G. S. Jenkins, L. O. Nyakiti, R. L. Myers-Ward, S. Li, J. Yan, D. K. Gaskill, T. E. Murphy, H. D. Drew, M. S. Fuhrer, *Nat. Nanotechnol.* **2014**, *9*, 814.
[26] S. Wall, S. Yang, L. Vidas, M. Chollet, J. M. Glownia, M. Kozina, T. Katayama, T. Henighan, M. Jiang, T. A. Miller, D. A. Reis, L. A. Boatner, O. Delaire, M. Trigo, *Science* **2018**, *362*, 572.
[27] I. A. Mogunov, S. Lysenko, A. E. Fedianin, F. E. Fernandez, A. Rua, A. J. Kent, A. V. Akimov, A. M. Kalashnikova, *Nat. Commun.* **2020**, *11*, 1690.
[28] A. S. Johnson, D. Perez-Salinas, K. M. Siddiqui, S. Kim, S. Choi, K. Volckaert, P. E. Majchrzak, S. Ulstrup, N. Agarwal, K. Hallman, R. F. Haglund, C. M. Günther, B. Pfau, S. Eisebitt, D. Backes, F. Maccherozzi, A. Fitzpatrick, S. S. Dhesi, P. Gargiani, M. Valvidares, N. Artrith, F. de Groot, H. Choi, D. Jang, A. Katoch, S. Kwon, S. H. Park, H. Kim, S. E. Wall, *Nat. Phys.* **2022**, *19*, 215.
[29] H. W. Liu, W. H. Liu, Z. J. Suo, Z. Wang, J. W. Luo, S. S. Li, L. W. Wang, *Proc. Natl. Acad. Sci. USA* **2022**, *119*, 2122534119.
[30] J. Xu, D. Chen, S. Meng, *Sci. Adv.* **2022**, *8*, eadd2392.
[31] J. Del Valle, P. Salev, F. Tesler, N. M. Vargas, Y. Kalcheim, P. Wang, J. Trastoy, M. H. Lee, G. Kassabian, J. G. Ramirez, M. J. Rozenberg, I. K. Schuller, *Nature* **2019**, *569*, 388.
[32] C. Feng, B. W. Li, Y. Dong, X. D. Chen, Y. Zheng, Z. H. Wang, H. B. Lin, W. Jiang, S. C. Zhang, C. W. Zou, G. C. Guo, F. W. Sun, *Sci. Adv.* **2023**, *9*, eadg9376.
[33] M. W. Kim, Y. R. Jo, C. Lee, W. J. Moon, J. H. Shim, B. J. Kim, *Nano Lett.* **2020**, *20*, 2733.
[34] Y. Xin, L. Hu, S. Ruan, Z. Ye, Y.-J. Zeng, *J. Mater. Chem. C* **2020**, *8*, 11399.
[35] T. S. Kasırga, D. Sun, J. H. Park, J. M. Coy, Z. Fei, X. Xu, D. H. Cobden, *Nat. Nanotechnol.* **2012**, *7*, 723.
[36] W. Liu, J. H. Lv, L. Peng, H. W. Guo, C. Liu, Y. L. Liu, W. Li, L. F. Li, L. X. Liu, P. Q. Wang, S. C. Bodepudi, K. Shehzad, G. H. Hu, K. H. Liu, Z. P. Sun, T. Hasan, Y. Xu, X. M. Wang, C. Gao, B. Y., X. F. Duan, *Nat. Electron.* **2022**, *5*, 281.
[37] M. Massicotte, P. Schmidt, F. Vialla, K. Watanabe, T. Taniguchi, K. J. Tielrooij, F. H. Koppens, *Nat. Commun.* **2016**, *7*, 12174.
[38] W. Zhang, J. K. Huang, C. H. Chen, Y. H. Chang, Y. J. Cheng, L. J. Li, *Adv. Mater.* **2013**, *25*, 3456.
[39] T. Wan, B. Shao, S. Ma, Y. Zhou, Q. Li, Y. Chai, *Adv. Mater.* **2023**, *35*, 2203830.
[40] F. C. Zhou, Y. Chai, *Nat. Electron.* **2020**, *3*, 664.
[41] S. Lysenko, V. Vikhnin, F. Fernandez, A. Rua, H. Liu, *Phys. Rev. B* **2007**, *75*, 075109.
[42] H. T. Kim, B. G. Chae, D. H. Youn, G. Kim, K. Y. Kang, S. J. Lee, K. Kim, Y. S. Lim, *Appl. Phys. Lett.* **2005**, *86*, 242101.
[43] Y. Chen, Y. Zhang, Z. Wang, T. Zhan, Y. C. Wang, H. Zou, H. Ren, G. Zhang, C. Zou, Z. L. Wang, *Adv. Mater.* **2018**, *30*, 1803580.
[44] Z. Li, J. Wu, Z. Hu, Y. Lin, Q. Chen, Y. Guo, Y. Liu, Y. Zhao, J. Peng, W. Chu, C. Wu, Y. Xie, *Nat. Commun.* **2017**, *8*, 15561.
[45] Y. Zhang, Y. Meng, L. Wang, C. Lan, Q. Quan, W. Wang, Z. Lai, W. Wang, Y. Li, D. Yin, D. Li, P. Xie, D. Chen, Z. Yang, S. Yip, Y. Lu, C. Y. Wong, J. C. Ho, *Nat. Commun.* **2024**, *15*, 728.
[46] X. Lu, P. Jiang, X. Bao, *Nat. Commun.* **2019**, *10*, 138.
[47] Y. J. Fang, A. Armin, P. Meredith, J. S. Huang, *Nat. Photonics* **2019**, *13*, https://doi.org/10.1038/s41566-018-0288-z.
[48] Y. C. Hou, C. C. Wu, X. Huang, D. Yang, T. Ye, J. Yoon, R. Sriramdas, K. Wang, S. Priya, *Adv. Funct. Mater.* **2021**, *31*, 2007016.
[49] Y. Chen, C. Tan, Z. Wang, J. Miao, X. Ge, T. Zhao, K. Liao, H. Ge, Y. Wang, F. Wang, Y. Zhou, P. Wang, X. Zhou, C. Shan, H. Peng, W. Hu, *Sci. Adv.* **2022**, *8*, eabq1781.
[50] W. Jiang, T. Zheng, B. Wu, H. Jiao, X. Wang, Y. Chen, X. Zhang, M. Peng, H. Wang, T. Lin, H. Shen, J. Ge, W. Hu, X. Xu, X. Meng, J. Chu, J. Wang, *Light Sci. Appl.* **2020**, *9*, 160.
[51] M. Dai, C. Wang, B. Qiang, F. Wang, M. Ye, S. Han, Y. Luo, Q. J. Wang, *Nat. Commun.* **2022**, *13*, 4560.
[52] D. Y. Fu, K. Liu, T. Tao, K. Lo, C. Cheng, B. Liu, R. Zhang, H. A. Bechtel, J. Q. Wu, *J. Appl. Phys.* **2013**, *113*, 043707.
[53] M. Schrade, H. Fjeld, T. Norby, T. G. Finstad, *Rev. Sci. Instrum.* **2014**, *85*, 103906.
[54] V. Linseis, F. Völklein, H. Reith, K. Nielsch, P. Woias, *Mater. Today-Proc.* **2019**, *8*, 517.
[55] M. Kockert, R. Mitdank, A. Zykov, S. Kowarik, S. F. Fischer, *J. Appl. Phys.* **2019**, *126*, 105106.
[56] X. H. Meng, Y. H. Du, W. B. Wu, N. B. Joseph, X. Deng, J. J. Wang, J. W. Ma, Z. P. Shi, B. L. Liu, Y. J. Ma, F. Y. Yue, N. Zhong, P. H. Xiang, C. Zhang, C. G. Duan, A. Narayan, Z. R. Sun, J. H. Chu, X. Yuan, *Adv. Sci.* **2023**, *10*, 2300413.